

# 1 **Modelling 3D permeability distribution in alluvial fans using facies architecture and** 2 **geophysical acquisitions**

3 Lin Zhu <sup>1</sup>, Huili Gong <sup>1</sup>, Zhenxue Dai <sup>2</sup>, Gaoxuan Guo <sup>3</sup>, Pietro Teatini <sup>4</sup>

4 <sup>1</sup>College of Resource Environment and Tourism, Capital Normal University, Laboratory Cultivation Base  
5 of Environment Process and Digital Simulation, Beijing, China

6 <sup>2</sup>Earth and Environmental Sciences Division, Los Alamos National Laboratory, Los Alamos, New  
7 Mexico, United States

8 <sup>3</sup> Beijing Institute of Hydrogeology and Engineering Geology, Beijing, China

9 <sup>4</sup> Department of Civil, Environmental and Architectural Engineering, University of Padova, Italy

10 *Correspondence to:* Lin Zhu [hi-zhulin@163.com](mailto:hi-zhulin@163.com); Huili Gong [gonghl@263.com](mailto:gonghl@263.com)

11

12 **Abstract.** Alluvial fans are highly heterogeneous in hydraulic properties due to complex depositional  
13 processes, which make it difficult to characterize the spatial distribution of the hydraulic conductivity ( $K$ ).  
14 An original methodology is developed to identify the spatial statistical parameters (mean, variance,  
15 correlation range) of the hydraulic conductivity in a three-dimensional setting by using geological and  
16 geophysical data. More specifically, a large number of inexpensive vertical electric soundings (properly  
17 calibrated through a few more-detail investigations as well logs) is integrated with a facies model  
18 developed from borehole lithologic data to simulate the  $\log_{10}(K)$  continuous distributions in multiple-zone  
19 heterogeneous alluvial megafans. The Chaobai River alluvial fan in the Beijing Plain, China, is used as  
20 an example to test the proposed approach. Due to the non-stationary property of the  $K$  distribution in the  
21 alluvial fan, a multi-zone parameterization approach is applied to analyze the conductivity statistical  
22 properties of different hydrofacies in the various zones. The composite variance in each zone is computed  
23 to describe the evolution of the conductivity along the flow direction. Consistently with the scales of the  
24 sedimentary transport energy, the results show that conductivity variances of fine sand, medium-coarse  
25 sand, and gravel decrease from the upper (Zone 1) to the lower (Zone 3) portion along the flow direction.  
26 In Zone 1, sediments were moved by higher-energy flooding, which induces poor sorting and larger  
27 conductivity variances. The composite variance confirms this feature with statistically different facies

28 from Zone 1 to Zone 3. The results of this study provide insights to improve our understanding on  
29 conductivity heterogeneity and a method for characterizing the spatial distribution of  $K$  in alluvial fans.  
30

## 31 **1 Introduction**

32 Alluvial fans usually house valuable groundwater resources because of significant water storage and  
33 favorable recharge conditions. Sedimentary processes forming alluvial fans are responsible for their  
34 complex long-term evolution. Usually, the coarsest material (gravel) is deposited in the upper fan, with  
35 the gravel passing into sand in the middle of the fan and then into silt and clay in the tail. A high  
36 heterogeneity characterizes the deposit distribution because of the shifting over time of the sediment-  
37 transporting streams (Zappa et al., 2006; Weissmann et al., 1999).

38 Hydraulic conductivity distributions in alluvial fans can be assigned according to the various hydrofacies  
39 simulated by conditional indicator geostatistical methods (Eggleston and Rojstaczer 1998; Fogg et al.,  
40 1998; Weissmann and Fogg, 1999; Weissmann et al., 2002a, 2002b; Ritzi et al., 2004, 2006; Proce et al.,  
41 2004; Dai et al., 2005; Harp et al., 2008; Hinnell et al., 2010; Maghrebi et al., 2015; Soltanian et al., 2015;  
42 Zhu et al., 2015a). However, the geostatistical methods require the stationary assumption, i.e. the  
43 distribution of the volumetric proportions and correlation lengths of hydrofacies converge to their mean  
44 values in the simulation domain. The hydrofacies and hydraulic conductivity ( $K$ ) distributions in alluvial  
45 fans are generally non-stationary (Weissmann et al., 1999; Anderson, 2007; Weissmann et al., 2010, 2013;  
46 Zhu et al., 2016a). Hence, the use of these methods may cause large characterization errors and add  
47 significant uncertainty to the predictions achieved by groundwater flow and contaminant transport models  
48 (Eggleston and Rojstaczer 1998; Irving and Singha 2010; Dai et al., 2014a). Zhu et al., (2016a) adopted

49 a local-stationary assumption by dividing the alluvial fan into three zones along the flow direction of the  
50 Chaobai River, China. The zones were properly detected based on the statistical facies distribution. Then,  
51 the indicator simulation method was applied to each zone and the simulated hydrofacies distribution in  
52 the three zones was used to guide modelling the  $K$  distribution.

53 Hydraulic conductivity of granular deposits generally varies with grain size, porosity, and sorting.  
54 Traditional methods for  $K$  estimate, e.g. well test, permeameter measurements, and grain-size analyses  
55 (Niwas et al., 2011), are very expensive, time-consuming, and make difficult to provide representative  
56 and sufficient field data for addressing spatial variations of conductivity. Recently, data fusion techniques  
57 have been developed for coupled inversion of multi-source data to estimate  $K$  distributions for  
58 groundwater numerical modeling. Geophysical data (such as surface electric resistivity and various  
59 logging data) are relatively inexpensive and can provide considerable information for characterizing  
60 subsurface heterogeneous properties (Hubbard et al., 2001; Yeh et al., 2002; Dai et al., 2004a; Morin  
61 2006; Sikandar et al., 2010; Bevington et al., 2016). Electric resistivity data have been proven useful to  
62 derive sediment porosity distributions (Niwas and Singhal 1985; Niwas et al., 2011; Niwas and Celik  
63 2012; Zhu et al., 2016b). Zhu et al. (2016b) simulated the spatial distributions of hydraulic conductivity  
64 by combing the interpolated resistivity on basis of VES and the stochastic simulated facies through  
65 empirical equation, in which the hydraulic conductivity was converted from the porosity data calculated  
66 from resistivity measurements and the grain size.

67 This study proposes a novel approach to reconstruct the three-dimensional configuration of conductivity  
68 in alluvial fans by combining the hydrofacies spatial heterogeneity provided by a multi-zone transition  
69 probability model with hydrogeological and hydrogeophysical measurements, in particular inexpensive

70 vertical electrical soundings (VES) properly calibrated through resistivity logs acquired in a few  
71 wellbores. We assume the  $K$  distributions are local-stationary, i.e. the mean and variance of log  
72 conductivity are convergent in each hydrofacies and in each local zone. Therefore, we can compute the  
73  $\log_{10}(K)$  semivariogram in each hydrofacies and in each zone. The spatial structure features of hydraulic  
74 conductivity deduced from semivariograms are used during the geostatistical simulation processes of the  
75 hydraulic conductivity. The Chaobai alluvial fan (or called “megafan” as defined by Leier et al. (2005)  
76 and Hartley et al. (2010) for very large alluvial fans) in the northern Beijing Plain, China, was selected as  
77 study area to test the proposed integrated approach.

78

## 79 **2 Material and Methods**

### 80 **2.1 Study area**

81 The study area belongs to the Chaobai River alluvial fan (or megafan), in the northern Beijing Plain  
82 (northern latitude  $40^{\circ}$ - $40^{\circ}30'$ , eastern longitude  $116^{\circ}30'$ - $117^{\circ}$ ), with an area of  $1,150 \text{ km}^2$  (Fig. 1a). The  
83 Chaobai River is the second largest river flowing through the Beijing Plain from north to south. The  
84 ground elevation decreases southward with an average 2‰ slope. Quaternary sediments were mainly  
85 deposited by flooding events with turbulent flow and consist of porous strata containing groundwater.  
86 The aquifer system in the alluvial fan can be divided into three zones according to the lithological features  
87 (Fig. 1): an upper fan zone (or Zone 1) with coarse sediments (e.g., sandy-gravel aquifers), a middle upper  
88 fan zone (or Zone 2) where medium-coarse sediments (e.g., sandy-gravel to sandy-silt aquifers) were  
89 deposited, and a fine-sediment (e.g., sand and clay multiple aquifers) middle-lower fan zone (or Zone 3).

90 Four hydrofacies, including sub-clay and clay (C), fine sand (FS), medium-coarse sand (MS), and gravel  
91 (G), were classified based on the interpretations of the cores and textural description of almost 700  
92 boreholes (Zhu et al., 2015).

93 The study area is one of the most important regions for the supply of groundwater resource to Beijing.  
94 The Huairou emergency groundwater resource region (hereafter EGRR) with an area of 54 Km<sup>2</sup> is located  
95 in Zone 1. The total groundwater withdrawal amounted to 1.2×10<sup>8</sup> m<sup>3</sup> in 2003. Several well-fields  
96 belonging to the so-called "water supply factory" were drilled along the Chaobai River in Zone 1 and the  
97 upper Zone 2. Most of these well-fields were built in 1979 with a designed groundwater pumping volume  
98 of 1.6×10<sup>8</sup> m<sup>3</sup> per year. The average thickness of the exploited aquifer system is approximately 300 m.  
99 The long-term over-exploitation of the aquifer system has resulted in a serious drawdown of water levels,  
100 which has reduced the exploitable groundwater resources and induced geological disasters, mainly land  
101 subsidence, fault reactivation, and ground fissures (Cheng et al., 2015; Yang et al., 2015; Zhu et al., 2015).  
102 In 2010, the annual groundwater withdrawal at the EGRR and the water factory decreased to 0.86×10<sup>8</sup>  
103 m<sup>3</sup> and 0.65×10<sup>8</sup> m<sup>3</sup>, respectively.

104 The largest cumulative land subsidence from June 2003 to January 2010 was quantified in approximately  
105 340 mm by Zhu et al., (2013, 2015) in Tianzhu County to the south. The characterization of the  
106 distribution and spatial variability of the hydraulic conductivity is vital for an optimal use of the limited  
107 water resources in this area.

## 108 **2.2 Methodological approach**

109 Nowadays, a large set of hydraulic conductivity samples can be derived by integrating appropriate  
110 relations of various geological data, including hydrogeophysical measurements, borehole  
111 lithostratigraphies, and hydrogeological information (total dissolved solid TDS and groundwater level).  
112 These databases can be statistically processed to derive the spatial variation of  $\log_{10}(K)$  for various facies,  
113 including clay, fine sand, medium-coarse sand, and gravel.

114 In this paper, the statistical assessment is separately carried out for separated zones, building-up  
115 experimental semivariograms that are fitted with exponential models. The optimal parameters of these  
116 latter are estimated through a generalized output least squares (OLS) criterion. Then, the composite  
117 semivariograms are computed using a hierarchical sedimentary architecture (Ritzi et al., 2004; Dai et al.,  
118 2005) to obtain the  $K$  variance in each zone. Finally, the configuration of  $\log_{10}(K)$  is simulated through a  
119 multiple-zone sequential Gaussian algorithm with estimated statistic parameters reflecting the  $K$  spatial  
120 structures in the alluvial fan. Figure 2 shows the steps involved in the developed approach.

## 121 **2.3 Data set**

### 122 **2.3.1 Geophysical data**

123 Geophysical data include resistivity loggings and vertical electrical soundings. There are six well-electric  
124 logs continuously recording the formation resistivity versus depth. Five logs were collected in Zone 2 and  
125 one in Zone 3. Each well log has a lithological description, which helps to relate the resistivity values to  
126 the corresponding facies.

127 The average resistivity of G is the largest, with a value of  $198 \Omega \text{ m}$ , and that of C is the smallest with a  
128 value of  $24 \Omega \text{ m}$ . Figure 3 compares the outcome of logging data in term of resistivity versus depth and

129 the corresponding stratigraphy, where the groundwater depth is 12 m. The log was acquired in the eastern  
130 part of Zone 2. The average resistivity from 32.4 m to 40.5 m depth, where the sediments are mainly G  
131 and MS, is 70.8  $\Omega$  m. The resistivity curve shows two evident peaks from 97 m to 102 m and between 81  
132 m and 84.5 m depth, where the MS is located.

133 The C resistivity is relatively low due to the good intrinsic electrical conductivity of this facies. For  
134 example from 16.5 m to 23.5 m depth, where C is the prevalent facies, a low resistivity equal to 27.2  $\Omega$   
135 m is recorded. Since a hydrofacies with a smaller grain size has a greater total surface area, the resistivity  
136 difference can partially reflect the distributions of particle sizes and the hydrofacies composition. Since  
137 the obtained resistivity is the apparent resistivity, we used the resistivity located in the middle of the facies  
138 block, where the resistivity is approximate to the real resistivity.

139 Vertical electrical soundings (VES) using the Schlumberger electrode configuration were carried out by  
140 the Beijing Institute of Hydrogeology and Engineering Geology (BIHEG). A number of 113 detecting  
141 positions were selected, with a maximum half current electrode space equal to 340 m and the potential  
142 electrode space ranging from 1 to 30 m. All the sounding data (1356 VES measurements) recorded the  
143 apparent resistivity of the porous medium. These data were inverted to real resistivity using the nonlinear  
144 Occam inversion method (Constable et al., 1987), with a low root mean square relative error of 2%. Figure  
145 4 shows the layered structure fitting model of resistivity and the borehole lithologic observations. The  
146 inversed resistivity generally reflects the difference of facies: the thick gravel layer has larger resistivity  
147 while the fine sand and clay layers have relatively smaller resistivity.

### 148 **2.3.2 Geological and hydrogeological data**

149 Almost 700 borehole lithologic logs were collected in the study area. The sedimentary deposits show large  
150 heterogeneity from the upper to the lower fan zone. In Zone 1, the dominant facies is G with a volumetric  
151 proportion of 53%. The volumetric proportion of C is 16%. In Zone 2, the volumetric proportion of C  
152 increases to 40%, while that of G decreases sharply to 24%. In Zone 3, the proportion of G decreases  
153 further to 6% and that of C increases to 50% (Table 1). More detailed information is given in Zhu et al.,  
154 (2016a). The lithological information in a buffer zone of 200 m around the VES locations has been used  
155 to represent the actual facies distribution in the area surrounding the sites of the geophysical acquisitions.  
156 A number of 35 hydrochemistry measurements with a depth from 20 m to 270 m were obtained throughout  
157 the area. The minimum, maximum and average TDS values are 423 mg/l at the depth of 180 m, 943 mg/l  
158 at the depth of 50 m, and 692 mg/l, respectively. Generally, the TDS is very low with the higher values  
159 measured in the south-western part of the study area. Because of the relatively small dataset and the  
160 observed low variability, in this paper the TDS variation in the vertical direction has been neglected. A  
161 TDS map was obtained by interpolating the available records using an Ordinary Kriging method with a  
162 spherical semivariogram model.

163 A large number of depth of water level measurements were also collected to map the thickness of the  
164 unsaturated unit. The TDS and groundwater level at each VES and resistivity log location were derived  
165 from the interpolated surfaces.

### 166 **2.3.3 Hydraulic conductivity estimates from geophysical acquisitions**

167 The hydraulic conductivity  $K$  was estimated using the Kozeny-Carman equation:

$$168 \quad K(x, y, z) = \frac{\delta g}{\mu} \times \frac{d_{(x,y,z)}^2}{180} \frac{\phi_{(x,y,z)}^3}{(1-\phi_{(x,y,z)})^2} \quad (1)$$

169 which is widely accepted to derive the hydraulic conductivity from grain size and porosity (Soupios et  
 170 al., 2007; Utom et al., 2013; Khalil et al., 2013; Zhu et al., 2016). In Eq. (1),  $d_{(x,y,z)}$  is the median grain  
 171 diameter (D50, mm) at location  $(x,y,z)$ , which was determined according to the lithology information (or  
 172 lithological descriptions and grain size distributions),  $g$  is gravity,  $\mu$  the kinematic viscosity (kg/(m·s)),  $\delta$   
 173 the fluid density, and  $\phi_{(x,y,z)}$  the porosity.  $\phi$  was estimated using Archie's law (Eq. (2)), which relates the  
 174 bulk resistivity of granular medium to porosity:

$$\rho = \alpha \rho_w \phi^{-m} s_w^{-n} \quad (2)$$

175 where  $\rho$  is the saturated formation resistivity ( $\Omega$  m),  $\alpha$  the pore-geometry coefficient associated with the  
 176 medium ( $0.5 \leq \alpha \leq 2.5$ ),  $m$  the cementation factor ( $1.3 \leq m \leq 2.5$ ) (Massoud et al., 2010; Khalil and Santos  
 177 2013).  $\alpha$  is set as 1. In the upper part of alluvial (Zone 1 and Zone 2)  $m$  is set as 1.3 due to the sand is  
 178 unconsolidated. In Zone 3  $m$  is set as 1.7 which reflects slightly cemented sandstones (Niwas et al. 2011).  
 179  $s_w$  the water saturation, and  $n$  the saturation index. The pore fluid resistivity ( $\Omega$  m)  $\rho_w$  is calculated using  
 180 the following experimental relation:

$$\rho_w = \frac{5.6(\text{TDS})^b}{1 + \beta(t-18)} \quad (3)$$

181 with TDS in (g/L), temperature  $t$  in ( $^{\circ}\text{C}$ ),  $b$  and  $\beta$  being constant parameters (Wu et al., 2003). For the  
 182 most common electrolytes,  $b = -0.95$  and  $\beta = 0.025$ . Note that the parameters associated with equations  
 183 (2) and (3) are site specific and application these equations to other sites will need re-adjust the related  
 184 parameters.

187 The logarithmically transformed values of the estimated hydraulic conductivity ( $\log_{10}(K)$ ) were used for  
188 the geostatistical analysis because of its normal distribution (Neuman, 1990). The histograms of  $\log_{10}(K)$   
189 values within each facies is in Fig. 5. There are 102, 2077, and 1716 conductivity samples in Zone 1,  
190 Zone 2, and Zone 3, respectively. Considering that Archie's law can only be used for clay-free granular  
191 sediments, the  $K$  values of C were not estimated in this study. Based on the lithological description  
192 information of borehole data, it has been reasonably assumed that clay fraction is negligible in G, MS,  
193 and FS facies. The statistics of  $\log_{10}(K)$  for the three facies in three zones are listed in Table 2. The mean  
194  $\log_{10}(K)$  values decrease from Zone 1 to Zone 3, consistently with the sedimentary transport processes in  
195 the alluvial fan. In the upper region (Zone 1), high water flowing energy made the deposits consisted  
196 mainly of larger-grained particles and the coarse-grained sediments are dominant. In the southern part  
197 (Zone 3), the deposits change to relatively fine-grained particles. The mean  $\log_{10}(K)$  of gravel is greater  
198 than 2.4 ( $\log(\text{m/d})$ ) and that of fine sand is less than 0.2 ( $\log(\text{m/d})$ ). The lithological information at the  
199 depth of the conductivity samples shows that volumetric proportions of FS and MS increase and that of  
200 G decreases from Zone 1 to Zone 3. The results are consistent with the statistic outputs deduced from 694  
201 borehole data by Zhu et al., (2016a).

## 202 **2.4 Statistical Methods**

### 203 **2.4.1 Semivariogram of hydraulic conductivity**

204 Semivariogram describes the degree of spatial dependence of a spatial random field or stochastic process.  
205 It is a concise and unbiased characterization of the spatial structure of regionalized variables, which is  
206 important in Kriging interpolations and conditional simulations. The experimental semivariogram:

207 
$$\hat{r}_k(h_\varphi) = \frac{1}{2N(h)} \sum_{(o,p) \in N(h)} (Y(z_o) - Y(z_p))^2 \quad (4)$$

208 can be fitted by an exponential model (e.g., Dai et al., 2014b):

209 
$$r_k(h_\varphi) = \sigma^2 (1 - e^{-\frac{3h}{\lambda}}) \quad (5)$$

210 where  $\hat{r}_k(h_\varphi)$  and  $r_k(h_\varphi)$  are the experimental and model semivariograms of log conductivity  $Y$  for the  
 211  $k^{th}$  facies at a lag distance  $h$  along the  $\varphi$  direction. In this paper we calculate the semivariograms in the  
 212 vertical and dip directions.  $N(h)$  is the number of pair measuring points  $z_o$  and  $z_p$  separated by a  $h$  lag  
 213 distance,  $\sigma^2$  is the variance, and  $\lambda$  the correlation range.

214 The variance and range were optimized using the least-squares criterion, which was solved by the  
 215 modified Gauss-Newton-Levenberg-Marquardt method (Clifton and Neuman, 1982; Dai et al., 2012).

216 The sensitivity equation method was derived to compute the Jacobian matrix for iteratively solving the  
 217 gradient-based optimization problem (Samper and Neuman 1986; Carrera and Neuman 1986; Dai and  
 218 Samper, 2004; Samper et al., 2006; Yang et al., 2014; Zhu et al., 2016a). The two sensitivity coefficients

219  $\frac{\partial r_k}{\partial \sigma^2}$  and  $\frac{\partial r_k}{\partial \lambda}$  are the partial derivatives of the semivariogram with respect to variance and range:

220 
$$\frac{\partial r_k}{\partial \sigma^2} = 1 - e^{-\frac{3h}{\lambda}} \quad (6)$$

221 
$$\frac{\partial r_k}{\partial \lambda} = -\sigma^2 \cdot 3h \cdot e^{-\frac{3h}{\lambda}} \cdot \lambda^{-2} \quad (7)$$

222

223 **2.4.2 Composite semivariogram of log conductivity**

224 Once the facies semivariograms were obtained in each zone, the composite semivariogram  $\gamma(h)$  could be  
225 calculated through the following equation (e.g., Ritzi et al., 2004):

$$226 \quad \gamma(h_\varphi) = \sum_{k=1}^M \sum_{i=1}^M r_{ki}(h_\varphi) p_k t_{ki}(h_\varphi) \quad (8)$$

227 where  $p_k$  and  $t_{ki}(h_\varphi)$  are the volumetric proportion of facies  $k$  and the transition probability from facies  
228  $k$  to facies  $i$  in the  $\varphi$  direction with a  $h$  lag distance, respectively. Equation 8 delineates the composite  
229 semivarigoram with respect to the individual facies semivariogram and transition probability. The general  
230 shape function and range of the composite semivarigoram can be obtained from individual facies mean  
231 length and volumetric proportion with the methods described in Dai et al., (2005).

232 The transition probability  $t_{ki}(h_\varphi)$  has an analytical solution as derived by Dai et al., (2007):

$$233 \quad t_{ki}(h_\varphi) = p_k + (\delta_{ki} - p_k) \cdot \exp\left(\frac{h_\varphi}{\lambda_\varphi}\right) \quad (9)$$

234 where  $\delta_{ki}$  is the Kronecker delta and  $\lambda_\varphi$  is the integral scale in the direction of  $\varphi$ . A geostatistical modeling  
235 tool GEOST (Dai et al., 2014b) modified from the Geostatistical Software Library (Deutsch and Journel,  
236 1992) and TPROGS (Carle and Fogg, 1997) was employed to compute the sample transition probabilities  
237 in each zone. The parameters  $p_k$  and  $\lambda_\varphi$  were optimally estimated through a modified Gauss-Newton-  
238 Levenberg-Marquardt method. More details are provided by Zhu et al., (2016a). The composite  
239 semivariograms for different zones can help us to understand the heterogeneity variations from the upper  
240 to lower part of the alluvial fan, as well as the stationary property (local versus regional) of the facies and  
241 hydraulic conductivity distributions.

### 242 **2.4.3 Sequential Gaussian simulation**

243 The Sequential Gaussian simulation (SGSIM) is a widely used stochastic simulation method to create  
244 numerical model of continuous variables based on the Gaussian probability density function. The process  
245 is assumed to be a stationary and ergodic random process (Deutsch and Journel, 1992; Dimitrakopoulos  
246 and Luo, 2004). This method can preserve the variance and correlation range observed in spatial samples.  
247 SGSIM provides a standardized normal continuous distribution of the simulated variable.

248 With the assumption that the log conductivity distributions are stationary within each zone, we used  
249 SGSIM simulator implemented into GEOST to model the  $\log_{10}(K)$  continuous configuration under a  
250 multiple-zone framework. The conductivity of the FS, MS, and G facies in each zone was simulated  
251 sequentially using the structure characteristics of the semivariograms.

252 Finally, the three-dimensional conductivity configuration was derived by combining the stochastic  
253 simulated facies (Zhu et al., 2016a) with the SGSIM conductivity distribution and the mean  $\log_{10}(K)$  of  
254 the various facies in each zone (Table 2). In detail, since each cell is characterized by specific facies and  
255 zone indices, its conductivity was assigned using the corresponding (in relation to the facies and the zone)  
256 3D SGSIM outcome in that position. Note that The hydrofacies (e.g., C, FS, MS and G) are defined  
257 qualitatively based on the sedimentary structures, borehole lithological descriptions, and grain sizes,  
258 while the conductivity samples are then deduced from geophysical measurements for each facies at each  
259 zone. Since the clay contents from zone 1 to zone 3 are increased due to the changes in the sediment  
260 transport conditions, for the same facies we also found this trend and the overall hydraulic conductivities  
261 are decreased from zone 1 to zone 3. Since sub-clay and clay are generally characterized by a low  
262 hydraulic conductivity value, a uniform  $K$  value equal to 0.0001 m/d was set to all the C cells.

### 263 **3 Results and Discussion**

### 264 **3.1 Variation of $\log_{10}(K)$ for the various facies**

265 The optimized vertical correlation range and variance of the log conductivity semivariogram (Eq. 5) are  
266 listed in Table 3, along with their 95% confidence intervals. The fitting between the experimental and the  
267 model semivariograms is the best in Zone 2 because of the abundant samples, while the fitting in Zone 1  
268 is the worst (Fig. 6). The fitting result of the semivariogram for the G facies is the worst in Zone 1. Two  
269 are the reasons: the first is the high variance of the log conductivity of gravel in this zone; the other is the  
270 limited number of samples (102 samples), which makes quite small the pair numbers within each lag  
271 spacing. Hence, the computed semivariogram is highly uncertain.

272 The variance of FS, MS, and G in the vertical direction decreases from Zone 1 to Zone 3. In the upper  
273 alluvial fan, sediments were deposited under multiple water flowing events and with poor sorting. The  
274 deposits consist of wide ranges of sediment categories and grain sizes. The variance of G is larger than  
275 1.5, which reflects the high heterogeneity of hydraulic conductivity in coarse deposits. The variances of  
276 FS and MS are smaller with values equal to 0.23 and 0.32, respectively. In Zone 3, these values decrease  
277 to 0.05 and 0.13, respectively, with that of G sharply decreasing to 0.62. In the middle-lower fan zone,  
278 the conductivity variation within each facies reduces gradually because the ground surface slope becomes  
279 smaller or flat, the sediment transport energy decreases, and the deposits within the three facies are well  
280 sorted.

281 Note that the ranges are correlated with the facies structure parameters such as the indicator correlation  
282 scale, mean thickness (or length), and volumetric proportion (Dai et al., 2004b; 2007). The estimated  
283 correlation ranges of FS, MS and G along the vertical direction in Zone 1 do not show big difference with

284 values equal to 6.0 m, 8.0 m and 6.5 m, respectively. Zone 2 was extended from the fan apex zone (Zone  
285 1) with much larger area, which allows for greater preservation potential of finer sediments (such as  
286 medium-coarse sand (MS), fine sand (FS), and clay or sub clay (C)) than the more proximal Zone 1.  
287 Therefore, in Zone 2 the volumetric proportions for these three facies increase while that of gravel  
288 decreases. The estimated ranges of G and MS are increased, respectively. In Zone 3, the range difference  
289 among the three facies decreases gradually. The range of FS is about 6.0 m, which is twice as much as  
290 that of MS. The spatial variation of the structure parameters of three facies causes the large changes of  
291 the correlation ranges from Zone 1 to Zone 3.

292 Due to the small number of conductivity samples in Zone 1, the variance of  $\log_{10}(K)$  along the dip  
293 direction is calculated only in Zone 2 and Zone 3 (Table 4, Fig. 7), as observed along the vertical direction.  
294 This phenomenon possibly reflects that sediment transport energy decrease along the flow direction.  
295 Lower energy flow in Zone 3 cause better sediment sorting and weak heterogeneity (or lower variance)  
296 in hydraulic conductivity.

### 297 **3.2 Compositd semivariogram of $\log_{10}(K)$**

298 The composite semivariogram in the vertical direction at each zone is calculated by Eq. (8), using the  
299 volume proportions (Table 1) and transition probability (Eq. (9)) with the same values of the lag distance  
300 used to compute the facies semivariograms (Fig. 8). The values of the optimized variance are 0.68, 0.11,  
301 and 0.03 in Zone 1, Zone 2, and Zone 3, respectively. The high flow energy and the large number of  
302 flooding events contributing to sediment deposition are the main causes of the high heterogeneity (largest  
303 variance) of the deposits in the upper part of the alluvial fan. The changes of variance between the three

304 zones support the utilization of the local-stationary assumption and simulation of multiple-zone based  
305 conductivity distributions for the Chaobai alluvial fan.

### 306 **3.3 Configuration of $\log_{10}(K)$**

307 The configuration of  $\log_{10}(K)$  in three dimensions is showed in Fig.9. The distribution of conductivity is  
308 generally consistent with that of the facies. Coarse units are more frequently distributed in the upper zone,  
309 which makes the average  $K$  is much larger in this zone than that in the lower part of the alluvial fan. The  
310 regions with high conductivity (red color in Fig. 8) in Zone 1 are more continuous than that in other parts.  
311 The adjacent cells with the smallest conductivity (blue color in Fig. 8) are obviously located mainly in  
312 Zone 3. The mean conductivity is smaller in the southern part of the study area, where the piezometric  
313 drawdowns in the multi-layer aquifer system were larger and the surface subsidence more serious (Zhu  
314 et al., 2013, 2015). Note that since we simulated the dip direction along one orientation (along the main  
315 water flow direction), the simulated facies in the fan apex did not show a radiating pattern. More  
316 information about simulating the radiating pattern can be found from Carle et al. (1997) and Fogg et al.  
317 (1998).

318 Based on the three dimensional  $K$  configuration, the average value of  $K$  in the depth range from 0 m to  
319 300 m amounts to 194 m/d, 25 m/d and 4 m/d in Zone 1, Zone 2, and Zone 3, respectively. These values  
320 are comparable with those provided by the Beijing Institute of Hydrogeology and Engineering Geology  
321 (2007) based on a number of pumping tests carried out over several years in the study area. In this BIHEG  
322 report the average value of  $K$  is  $>300$  m/d in Zone 1, between 30 and 100 m/d in Zone 2, and  $<30$  m/d  
323 in Zone 3 (Fig. 1b). The fact that the arithmetic average  $K$  values are gently smaller than these latter are

324 likely due to the fact that the outcome of pumping tests are generally more representative of coarser  
325 sediments.

326 Investigating the stochastic results along the vertical direction, it is interesting to notice that the average  
327  $K$  in deep units of Zone 1 and Zone 2 is smaller than that in the shallow strata. For example, in Zone 1  
328 the average  $K$  for the cells from 0 m to 100 m deep is 295 m/d, which is three times as much the value for  
329 the depth range between 200 m and 300 m. Conversely, no significant variation of  $K$  versus depth is  
330 observed in Zone 3, with only a small decrease of the average  $K$  from the deeper to the shallower units.

#### 331 **4 Conclusions**

332 This paper proposes a geostatistical method under a multiple zone framework, properly supported by a  
333 large number of geophysical investigations, to detect the distribution and the related variance of the  
334 hydraulic conductivity in three-dimensional domains. In particular, the optimized statistical parameters  
335 (e.g., log conductivity variance and correlation range) of semivariograms are estimated using the modified  
336 Gauss-Newton-Levenberg-Marquardt method. The Chaobai alluvial fan is used as a case study area.  
337 Multiple data including downhole resistivity logging data, vertical electric soundings, well-bore lithologic  
338 logs, TDS measurements, and depths to the water table are integrated to derive a dataset of conductivity  
339 values in a three-dimensional setting. Log conductivity semivariograms fitted with exponential functions  
340 were constructed for three facies, including fine sand, medium-coarse sand and gravel, in each of the three  
341 zones into which the Chaobai fan is divided to guarantee local stationarity of the statistical process. The  
342 composite semivariogram of the three facies has been derived for the two zones where a sufficiently large  
343 number of samples are available. The  $\log_{10}(K)$  configuration is simulated using the sequential Gaussian

344 simulation model based on statistic parameters of  $\log_{10}(K)$  and the structure suggested by a 3D hydrofacies  
345 simulation.

346 For the specific test case, the variance along the vertical direction of fine sand, medium-coarse sand, and  
347 gravel decreases from the upper part of the alluvial fan, where the values amount to 0.23, 0.32, and 1.60,  
348 to the lower portion of the Chaobai plan with values of 0.05, 0.126, and 0.62, respectively. This behavior  
349 reflects the higher transport energy in the upper alluvial fan that causes a poor sediment sorting. In the  
350 middle alluvial fan, the transport energy decreases and the sediments tend to be relatively well-sorted.  
351 The variance of the gravel is larger than that of other lithologies. The different flow energy significantly  
352 affected the coarse sediments in the vertical direction. Along the dip direction, the variance of three facies  
353 (gravel, medium-coarse sand and fine sand) in the middle fan is larger than that in the lower fan. The  
354 composite variance of  $\log_{10}(K)$  in the vertical direction shows that the large heterogeneity in the upper  
355 fan (with a value of 0.68) decreases in the lower zone.

356 The distribution of hydraulic conductivity is consistent with that of the facies. Hydraulic conductivity is  
357 much larger in the upper zone than that in the lower part of the alluvial fan. This result provides valuable  
358 insights for understanding the spatial variations of hydraulic conductivity and setting-up groundwater  
359 flow, transport, and land subsidence models in alluvial fans.

360 Concluding, it is worth highlighting that we depicted an original method to detect the variance and  
361 configuration of conductivity by fusing multiple-source data in three-dimensional domains. The proposed  
362 approach can be easily used to statistically characterize the hydraulic conductivity of the various alluvial  
363 fans that worldwide are strongly developed to provide high-quality water resources. We are aware of

364 some restrictions in the dataset available at the date for the Chaobai alluvial fan, for example the assumed  
365 uniform distribution of TDS versus depth and the relatively small number of the conductivity samples in  
366 the upper fan zone. Nonetheless, the proposed methodology will be re-applied in the near future as soon  
367 as new information will become available, thus allowing to improve the estimation accuracy of spatial  
368 statistics parameters and the configuration of hydraulic conductivity in this Quaternary system so  
369 important for the Beijing water supply.

### 370 **Data availability**

371 The geophysical measurements, borehole lithostratigraphies, and hydrogeological information in the  
372 north part of Beijing Plain can be partly accessible by contacting Beijing Institute of Hydrogeology and  
373 Engineering Geology.

### 374 **Author contribution**

375 Lin Zhu, Huili Gong and Zhenxue Dai derived the method of spatial variance and 3D configuration of  
376 conductivity, performed data analysis and wrote the draft manuscript. Gaoxuan Guo collected the  
377 geological and geophysical data, discussed the results. Pietro Teatini discussed the results, reviewed and  
378 revised the manuscript.

### 379 **Competing interests**

380 The authors declare that they have no conflict of interest.

### 381 **Acknowledgements**

382 This work was supported by the National Natural Science Foundation (No.41201420, 41130744) and  
383 Beijing Nova Program (No.Z111106054511097). Pietro Teatini was partially supported by the University  
384 of Padova, Italy, within the 2016 International Cooperation Program.

## 385 **References**

386 Anderson, M.P.: Introducing groundwater physics, *Phys. Today*, 42–47, 2007

387 Beijing Institute of Hydrogeology and Engineering Geology: Groundwater flow model and the potential  
388 groundwater resources in Beijing Plain, Internal Report, 60-64., 2007 (In Chinese)

389 Bevington, J., Piragnolo, D., Teatini, P., Vellidis, G., and Morari, F.: On the spatial variability of soil  
390 hydraulic properties in a Holocene coastal farmland, *Geoderma*, 262: 294-305,  
391 doi:10.1016/j.geoderma.2015.08.025, 2016.

392 Carle, S.F., and Fogg, G.E.: Modeling spatial variability with one and multidimensional continuous-lag  
393 Markov chain, *Math. Geol.*, 29: 891-918, doi: 10.1023/a:1022303706942, 1997.

394 Carrera, J., and Neuman, S.P.: Estimation of aquifer parameters under steady state and transient condition:  
395 2. Uniqueness, stability, and solution algorithms, *Water Resour. Res.*, 22, 211 – 227, doi:  
396 10.1029/wr022i002p00211, 1986.

397 Cheng, G., Wang, H., Luo, Y., and Guo, H.: Study of the deformation mechanism of the Gaoliying ground  
398 fissure: Prevention and Mitigation of Natural and Anthropogenic Hazards due to Land Subsidence - Proc.  
399 IX Int. Symp. on Land Subsidence, K. Daito et al. eds., Proc. IAHS, UK, 231-234, 2015.

400 Clifton, P.M., and Neuman, S.P.: Effects of kriging and inverse modeling on conditional simulation of  
401 the Avra Valley aquifer in southern Arizona, *Water Resour. Res.*, 18, 1215-1234, doi:  
402 10.1029/wr018i004p01215, 1982.

403 Constable, S.C., Parker, R.L., and Constable, C.G.: Occam's inversion: A practical algorithm for  
404 generating smooth models from electromagnetic sounding data, *Geophysics*, 52, 289-300, 1987.

405 Dai, Z., and Samper, J.: Inverse problem of multicomponent reactive chemical transport in porous media:  
406 Formulation and applications, *Water Resour. Res.*, 40, W07407, doi: 10.1029/2004wr003248, 2004.

407 Dai, Z., Ritzi, R., and Dominic, D.: Estimating parameters for hierarchical permeability correlation  
408 models. Aquifer Characterization, Bridge, J.S. and Hyndman, D.W. *SEPM Society for Sedimentary*  
409 *Geology*, USA, 41-54, doi: 10.2110/pec.04.80.0041, 2004a.

410 Dai, Z., Ritzi, R., Huang, C., Dominic, D., and Rubin, Y.: Transport in heterogeneous sediments with  
411 multimodal conductivity and hierarchical organization across scales, *J. of Hydrol.*, 294, 68-86, doi:  
412 10.1007/s00477-014-0922-3, 2004b.

413 Dai Z., Ritzi, R., and Dominic, D.: Improving permeability semivariograms with transition probability  
414 models of hierarchical sedimentary architecture derived from outcrop analog studies. *Water Resour. Res.*,  
415 14 W07032, doi: 10.1029/2004wr003515, 2005.

416 Dai, Z., Wolfsberg, A., Lu, Z., and Ritzi, R.: Representing aquifer architecture in macrodispersivity  
417 models with an analytical solution of the transition probability matrix. *Geophys. Res. Lett.*, 34, L20406,  
418 doi: 10.1029/2007GL031608, 2007.

419 Dai, Z., Wolfsberg, A., Reimus, P., Deng, H., Kwicklis, E., Ding, M., Ware, D., and Ye, M.: Identification  
420 of sorption processes and parameters for radionuclide transport in fractured rock, *J. Hydrol.*, 414-415,  
421 220-230, doi: 10.1016/j.jhydrol.2011.10.035, 2012.

422 Dai, Z., Viswanathan, H., Fessenden-Rahn, J., Middleton, R., Pan, F., Jia, W., Lee, S., McPherson, B.,  
423 Ampomah, W., and Grigg, R.: Uncertainty quantification for CO<sub>2</sub> sequestration and enhanced oil recovery,  
424 *Energy Procedia*, 63, 7685–7693, 2014a.

425 Dai, Z., Middleton, R., Viswanathan, H., Fessenden-Rahn, J., Bauman, J., Pawar, R., Lee, S., and  
426 McPherson, B.: An integrated framework for optimizing CO<sub>2</sub> sequestration and enhanced oil recovery.  
427 *Environ. Sci. Technol. Lett.*, 1, 49-54, doi: 10.1021/ez4001033, 2014b.

428 Deutsch, C.V., and Journel, A.G. *GSLIB: Geostatistical software library*, Oxford Univ. Press. New York,  
429 340, 1992.

430 Dimitrakopoulos, R., and Luo, X.: Generalized sequential Gaussian simulation on group size  $v$  and  
431 screen-effect approximations of large field simulations. *Math. Geol.*, 36, 567-590, doi:  
432 10.1023/b:matg.0000037737.11615.df, 2004.

433 Eggleston, J., and Rojstaczer, S.: Identification of large-scale hydraulic conductivity trends and the  
434 influence of trends on contaminant transport. *Water Resour. Res.*, 34, 2155-2186, doi:  
435 10.1029/98wr01475, 1998.

436 Fogg, G.E., Noyes, C.D., and Carle, S.F.: Geologically based model of heterogeneous hydraulic  
437 conductivity in an alluvial setting, *Hydrogeol. J.*, 6(1), 131-143, doi: 10.1007/s100400050139, 1998.

438 Harp, D., Dai, Z., Wolfsberg, A., and Vrugt, J.: Aquifer structure identification using stochastic inversion,  
439 *Geophys. Res. Lett.*, 35, L08404, doi: 10.1029/2008gl033585, 2008.

440 Hartley, A.J., Weissmann, G.S., Nichols, G.J., and Warwick, G.L., Distributive fluvial systems:  
441 characteristics, distribution, and controls on development, *J. of Sediment. Res.*, 79, 167-183, doi:  
442 10.2110/jsr.2010.016, 2010.

443 Hinnell, A.C., Ferre, T.P.A., Vrugt, J., Huisman, J.A., Moysey, S., Rings, J., and Kowalsky, M.B.:  
444 Improved extraction of hydrologic information from geophysical data through coupled hydrogeophysical  
445 inversion. *Water Resour. Res.*, 46, doi: 10.1029/2008wr007060, 2010.

446 Hubbard, S.S., Chen, J.S., Peterson, J., Majer, E.L., Williams, K.H., Swift, D.J., Mailloux, B., and Rubin,  
447 Y.: Hydrogeological characterization of the South Oyster Bacterial Transport site using geophysical data,  
448 *Water Resour. Res.*, 37, 2431-2456, doi: 10.1029/2001wr000279, 2001.

449 Irving, J., and Singha, K.: Stochastic inversion of tracer test and electrical geophysical data to  
450 estimate hydraulic conductivities, *Water Resour. Res.*, 46, W11514, doi: 10.1029/2009WR008340, 2010.

451 Khalil, M.A., and Santos, F.A.M.: Hydraulic conductivity estimation from resistivity logs: a case study  
452 in Nubian sandstone aquifer. *Arab. J. Geosci.*, 6, 205-212. doi: 10.1007/s12517-011-0343-2, 2013.

453 Leier, A.L., P. G. DeCelles, J. D. Pelletier, Mountains, monsoons, and megafans, *Geology*, 33, 289-292.  
454 doi: 10.1130/G21228.1, 2005.

455 Maghrebi, M., Jankovic, I., Weissmann, G.S., Matott, L.S., Allen-King, R.M., and Rabideau, A.J.,  
456 Contaminant tailing in highly heterogeneous porous formations: Sensitivity on model selection and  
457 material properties. *J. of Hydrol.*, 531, 149-160. doi: 10.1016/j.jhydrol.2015.07.015, 2015.

458 Massoud, U., Santos, F.A.M., Khalil, M. A., Taha, A., and Abbas, A. M.: Estimation of aquifer hydraulic  
459 parameters from surface geophysical measurements: a case study of the Upper Cretaceous aquifer, central  
460 Sinai, Egypt, *Hydrogeol. J.*, 18, 699-710, doi: 10.1007/s10040-009-0551-y, 2010.

461 Morin, R.H.: Negative correlation between porosity and hydraulic conductivity in sand-and-gravel  
462 aquifers at Cape Cod, Massachusetts, USA, *J. Hydrol.*, 316, 43-52, doi:10.1016/j.jhydrol.2005.04.013,  
463 2006.

464 Neuman, S.P.: Universal scaling of hydraulic conductivities and dispersivities in geologic media, *Water*  
465 *Resour. Res.*, 26, 1749-1758, 1990.

466 Niwas, S., and Singhal, D.C.: Aquifer transmissivity of porous media from resistivity data, *J. Hydrol.*, 82,  
467 143-153, doi: 10.1016/0022-1694(85)90050-2, 1985.

468 Niwas, S., Tezkan, B., and Israil, M.: Aquifer hydraulic conductivity estimation from surface  
469 geoelectrical measurements for Krauthausen test site, Germany, *Hydrogeol. J.*, 19, 307-315, doi:  
470 10.1007/s10040-010-0689-7, 2011.

471 Niwas, S., and Celik, M.: Equation estimation of porosity and hydraulic conductivity of Ruhrtal aquifer  
472 in Germany using near surface geophysics. *J. Appl. Geophys.*, 84, 77-85, doi:  
473 10.1016/j.jappgeo.2012.06.001, 2012.

474 Proce, C., Ritzi, R. W., Dominic, D., and Dai, Z.: Modeling multiscale heterogeneity and aquifer  
475 interconnectivity, *Ground Water*, 42, 658-670, 2004.

476 Ritzi R., Dai, Z., Dominic, D., Rubin Y.: Reply to comment by Shlomo P. Neuman on “Spatial correlation  
477 of permeability in cross-stratified sediment with hierarchical architecture”. *Water Resour. Res.*, 42,  
478 W05602, doi:10.1029/2005WR004402, 2006.

479 Ritzi R., Dai, Z., and Dominic, D.: Spatial correlation of permeability in cross-stratified sediment with  
480 hierarchical architecture. *Water Resour. Res.*, 40, W03513, doi: 10.1029/2003wr002420, 2004.

481 Samper, F.J., and Neuman, S.P.: Adjoint state equations for advective-dispersive transport: Proceeding  
482 of the 6<sup>th</sup> International Conference in Finite Elements in Water Resource, 423-437, New York, doi:  
483 10.1007/978-3-662-11744-6\_31, 1986.

484 Samper, J., Dai, Z., Molinero, J., García-Gutiérrez, M., Missana, T., and Mingarro, M.: Inverse modeling  
485 of tracer experiments in FEBEX compacted Ca-bentonite. *Physics and Chemistry of the Earth*, 31, 640-  
486 648, 2006.

487 Sikandar, P., Bakhsh, A., Arshad, M., and Rana, T.: The use of vertical electrical sounding resistivity  
488 method for the location of low salinity groundwater for irrigation in Chaj and Rachna Doabs, *Environ.*  
489 *Earth Sci.*, 60, 1113-1129, doi: 10.1007/s12665-009-0255-6, 2010.

490 Soltanian, M.R., Ritzi, R.W., Huang, C.C., and Dai, Z.: Relating reactive solute transport to hierarchical  
491 and multiscale sedimentary architecture in a Lagrangian-based transport model: 2: Particle displacement  
492 variance. *Water Resour. Res.*, 51, 1601-1618, doi: 10.1002/2014wr016354, 2015.

493 Soupios, P.M., Kouli, M., Vallianatos, F., Vafidis, A., and Stavroulakis, G.: Estimation of aquifer  
494 hydraulic parameters from surficial geophysical methods: A case study of Keritis Basin in Chania (Crete-  
495 Greece), *J. Hydrol.*, 338, 122-131, doi: 10.1016/j.jhydrol.2007.02.028, 2007.

496 Utom, A.U., Odoh, B.I., Egboka, B.C.E., Egboka, N.E., and Okeke, H.C.: Estimation of subsurface  
497 hydrological parameters around Akwuke, Enugu, Nigeria using surface resistivity measurements. *J.*  
498 *Geophys. Eng.*, 10, 025016, doi: 10.1088/1742-2132/10/2/025016, 2013.

499 Weissmann, G.S., and Fogg, G.E.: Multi-scale alluvial fan heterogeneity modeled with transition  
500 probability geostatistics in a sequence stratigraphic framework. *J. Hydrol.*, 226, 48–65, doi:  
501 10.1016/S0022-1694(99)00160-2, 1999.

502 Weissmann, G.S., S.F. Carle, G.E. Fogg, Three-dimensional hydrofacies modeling based on soil surveys  
503 and transition probability geostatistics, *Water Resour. Res.*, 35(6), 1761–1770, 1999.

504 Weissmann, G.S., Yong, Z., Fogg, G.E., Blake, R.G., Noyes, C.D., and Maley, M.: Modeling alluvial fan  
505 aquifer heterogeneity at multiple scales through stratigraphic assessment. Proceedings of the International

506 Groundwater Symposium: Bridging the gap between measurement and modeling in heterogeneous media,  
507 Lawrence Berkeley National Laboratory, Berkeley, California, p25-28, 2002a.

508 Weissmann, G.S., Mount, J.F., and Fogg, G.E.: Glacially driven cycles in accumulation space and  
509 sequence stratigraphy of a stream-dominated alluvial fan, San Joaquin Valley, California, USA, *J. of*  
510 *Sediment. Res.* 72 (2), 240-251, 2002b.

511 Weissmann, G.S., Hartley, A.J., Nichols, G.J., Scuderi, L.A., Olson, M., Buehler, H., and Banteah, R.,  
512 Fluvial form in modern continental sedimentary basins: the distributive fluvial system (DFS) paradigm:  
513 *Geology*, 38, 39-42, doi: 10.1130/G30242.1, 2010.

514 Weissmann, G.S., Hartley, A.J., Scuderi, L.A., Nichols, G.J., Davidson, S.K., Owen, A., Atchley, S.C.,  
515 Bhattacharyya, P., Chakraborty, T., Ghosh, P., Nordt, L.C., Michel, L., and Tabor, N.J., Prograding  
516 distributive fluvial systems – geomorphic models and ancient examples, in Driese, S.G., and Nordt, L.C.  
517 (eds), *New Frontiers in Paleopedology and Terrestrial Paleoclimatology*, SEPM Special Publication No.  
518 104, p. 131-147, 2013.

519 Wu, Y., Guo, J., and Qiang, J.: Assessing the total dissolved solid in groundwater on basis of resistivity.  
520 Conference on Groundwater Survey and Monitoring Technology, Baoding Hebei, China, 2003. (In  
521 Chinese)

522 Yang, C., Dai, Z., Romanak, K., Hovorka, S., and Trevino, R.: Inverse Modeling of Water-Rock-CO<sub>2</sub>  
523 Batch Experiments: Implications for Potential Impacts on Groundwater Resources at Carbon  
524 Sequestration Sites, *Environ. Sci. Technol.*, 48, 2798–2806, doi: 10.1021/es4041368, 2014.

525 Yang, Y., Luo, Y., Liu, M., Wang, R., and Wang, H.: Research of features related to land subsidence and  
526 ground fissure disasters in the Beijing Plain: Prevention and Mitigation of Natural and Anthropogenic  
527 Hazards due to Land Subsidence - Proc. IX Int. Symp. on Land Subsidence, K. Daito et al. eds., Proc.  
528 IAHS,UK, 372, 239-242, 2015.

529 Yeh, T.C., Liu, S., Glass, R.J., Baker, K., Brainard, J.R., Alumbaugh, D., and LaBrecque, D.: A  
530 geostatistically based inverse model for electrical resistivity surveys and its applications to vadose zone  
531 hydrology. *Water Resour. Res.*, 38, 1278, doi: 10.1029/2001wr001204, 2002.

532 Zappa, G., Bersezio, R., Felletti, F., and Giudici, M.: Modeling heterogeneity of gravel-sand, braided  
533 stream, alluvial aquifers at the facies scale. *J. Hydrol.*, 325,134-153, doi :10.1016/j.jhydrol.2005.10.016,  
534 2006.

535 Zhu, L., Gong, H., Li, X., Li, Y., Su, X., and Guo, G.: Comprehensive analysis and artificial intelligent  
536 simulation of land subsidence of Beijing, China. *Chin. Geogra. Sci.*, 23, 237–248, doi: 10.1007/s11769-  
537 013-0589-6, 2013.

538 Zhu, L., Gong, H., Li, X., Wang, R., Chen, B., Dai, Z., and Teatini, P.: Land subsidence due to  
539 groundwater withdrawal in the northern Beijing plain, China, *Eng. Geol.*, 193, 243-255, doi:  
540 10.1016/j.enggeo.2015.04.020, 2015.

541 Zhu, L., Dai, Z., Gong, H., Gable, C., and Teatini, P.: Statistic inversion of multi-zone transition  
542 probability models for aquifer characterization in alluvial fans. *Stoch. Environ. Res. Risk Assess.*, 30,  
543 1005-1016, doi: 10.1007/s00477-015-1089-2, 2016a.

544 Zhu, L., Gong, H., Chen, Y., Li, X., Chang, X., and Cui, Y.: Improved estimation of hydraulic  
545 conductivity by combining stochastically simulated hydrofacies with geophysical data. *Sci. Rep.*, 6, 22224,  
546 doi: 10.1038/srep22224, 2016b.

547 **Table 1 Values of the volumetric proportion for the various facies in three zones**

Zone	Sub-clay and clay	Fine sand	Medium-coarse sand	Gravel
Zone 1	0.166	0.234	0.067	0.533
Zone 2	0.409	0.286	0.065	0.240
Zone3	0.503	0.328	0.106	0.063

554

555

556

557 **Table 2 Statistical data of logarithm hydraulic conductivity ( $\log_{10}(m/d)$ ) in the three zones of the Chaobai**  
 558 **alluvial fan**

Zone	Parameter	Fine sand	Medium-coarse sand	Gravel
	<b>Mean</b>	<b>1.07</b>	<b>1.82</b>	<b>2.92</b>
Zone 1	Minimum	-0.94	1.22	2.26
	Maximum	1.65	2.45	3.66
	Proportion	0.36	0.12	0.32
	<b>Mean</b>	<b>0.42</b>	<b>1.17</b>	<b>2.65</b>
Zone 2	Minimum	-2.22	-0.23	0.95
	Maximum	1.22	2.07	3.38
	Proportion	0.23	0.14	0.31
	<b>Mean</b>	<b>0.17</b>	<b>0.81</b>	<b>2.48</b>
Zone 3	Minimum	-2.64	-0.78	0.34
	Maximum	0.72	1.43	3.21
	Proportion	0.35	0.17	0.12

559

560

561

562

563

**Table 3 Optimized parameters in the fitting exponential function of  $\log_{10}(K)$  semivariogram in vertical direction for the various facies and zones**

564

Zone	Parameter	Fine sand		Medium-coarse sand		Gravel	
		Estimated value	Confidence Interval (95%)	Estimated value	Confidence Interval (95%)	Estimated value	Confidence Interval (95%)
Zone 1	Variance	0.23	(0.19, 0.28)	0.32	(0.29, 0.34)	<b>1.60</b>	(1.41, 1.81)
	Range (m)	6.01	(2.01, 20.52)	8.01	(1.53, 14.67)	6.50	(6.5, 12.84)
Zone 2	Variance	0.069	(0.067, 0.070)	<b>0.14</b>	(0.13, 0.15)	<b>1.22</b>	(1.19, 1.24)
	Range (m)	3.13	(1.83, 4.42)	8.27	(3.61, 12.93)	15.0	(12.33, 17.67)
Zone3	Variance	0.05	(0.047, 0.053)	<b>0.126</b>	(0.118, 0.135)	<b>0.62</b>	(0.54, 0.7)
	Range (m)	6.52	(2.19, 10.85)	2.72	(0.20, 6.55)	5.98	(0.20, 15.63)

565

**Table 4 Variances of  $\log_{10}(K)$  of different facies along the dip direction in Zone 2 and Zone 3**

566

Zone		Fine sand	Medium-coarse sand	Gravel
Zone 2	Estimated value	<b>0.10</b>	<b>0.15</b>	<b>1.38</b>
	Confidence Interval (95%)	(0.059, 0.141)	(0.071, 0.228)	(1.14, 1.62)
Zone 3	Estimated value	<b>0.045</b>	<b>0.068</b>	<b>0.48</b>
	Confidence Interval (95%)	(0.030, 0.0607)	(0.043, 0.093)	(0.22, 0.73)

567

568 **Figure captions**

569 Figure 1 Chaobai alluvial fan in the north of Beijing Plain. (a) Location of the study area and distribution  
570 of the field data. (b) Map of the hydraulic conductivity issued by Beijing Institute of Hydrogeology and  
571 Engineering Geology (2007). The location of the study area is shown in the inset.

572 Figure 2 Flowchart of the geostatistical methodology

573 Figure 3 Typical depth behaviors of resistivity and corresponding stratigraphy in the eastern part of Zone  
574 2

575 Figure 4 Inversed resistivity and corresponding stratigraphy in Zone 1

576 Figure 5 Histograms of  $\log_{10}K$  for fine sand, medium-coarse sand and gravel

577 Figure 6 Experimental (circle symbol) and model (solid line) semivariogram along the vertical direction  
578 for the various hydrofacies in the three zones. Notice that the range in the y-axis differs for gravel  
579 lithology.

580 Figure 7 Experimental (circle symbol) and model (solid line) semivariogram along the dip direction for  
581 the various hydrofacies in Zone 2 and Zone 3. Notice that the range in the y-axis differs for gravel  
582 lithology.

583 Figure 8 Experimental (circle symbol) and model (solid line) composited semivariogram along the  
584 vertical direction for the three zones.

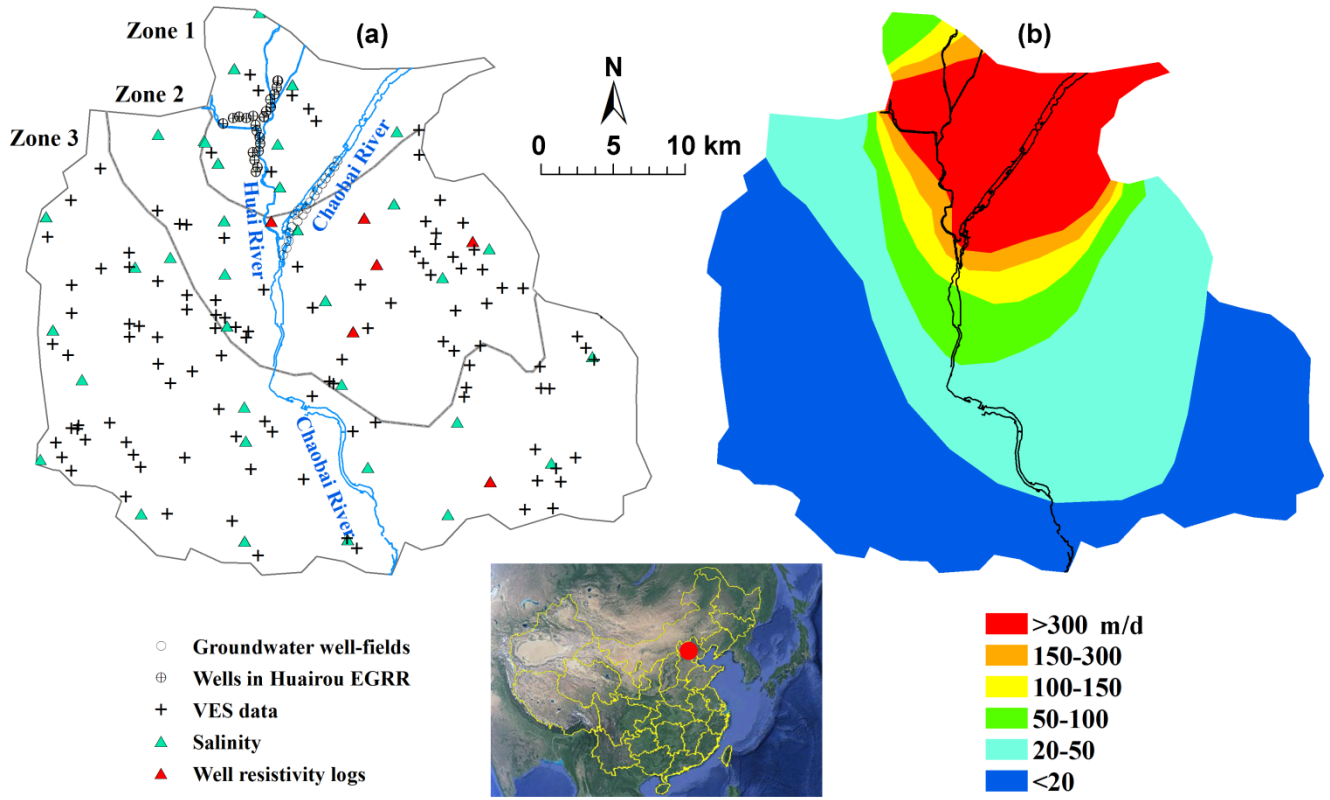
585 Figure 9 Distribution of hydrofacies (after Zhu et al., 2015a) and  $\log_{10}(K)$  in the three-dimensional domain  
586 representing the Chaobai alluvial fan: (a) axonometric projection of the three-dimensional system and (b)  
587 vertical sections along the A-A', B-B', C-C' and D-D' alignments. The vertical exaggeration is 25. The  
588 selected cell size is 300 m in north-south and east-west directions and 5 m in vertical direction, with a  
589 total number of 747, 540 cells. The thickness of the simulated domain is 300 m.

590

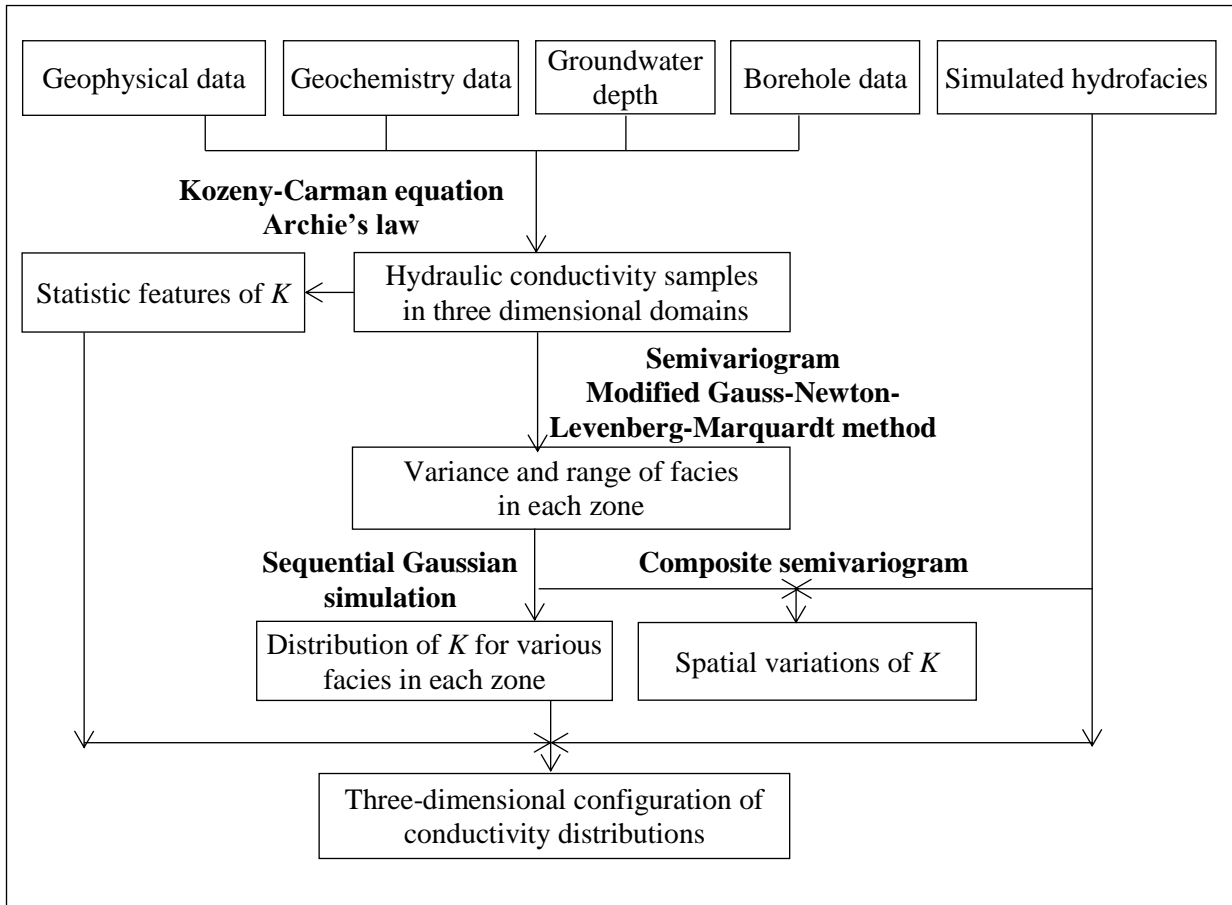
591

592

593



597



598

599

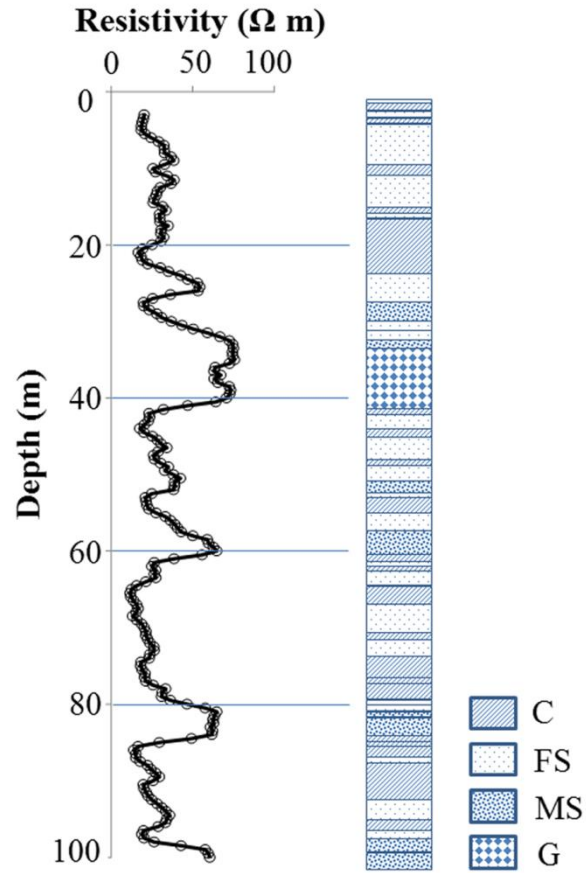
600

601

602

603 **Figure3**

604



605

606

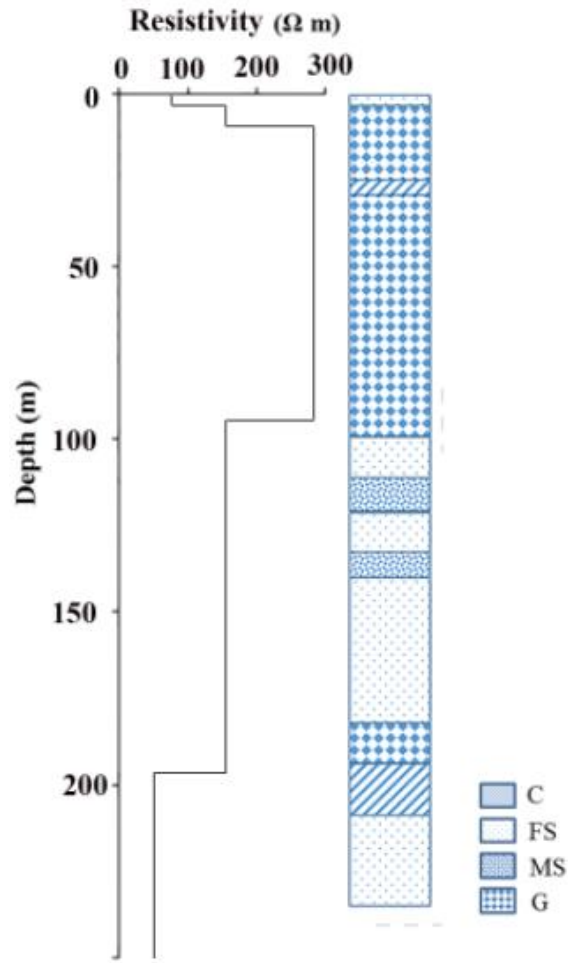
607

608

609

610

611 **Figure 4**



612

613

614

615

616

617

618

619

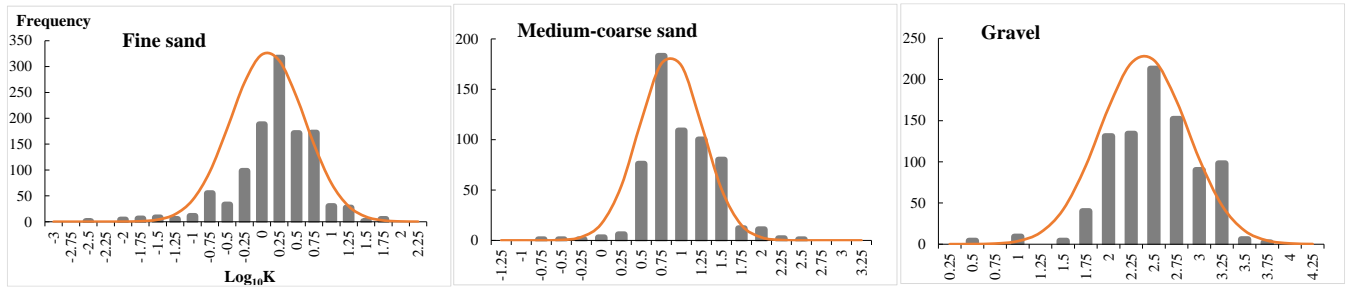
620

621

622 **Figure 5**

623

624



625

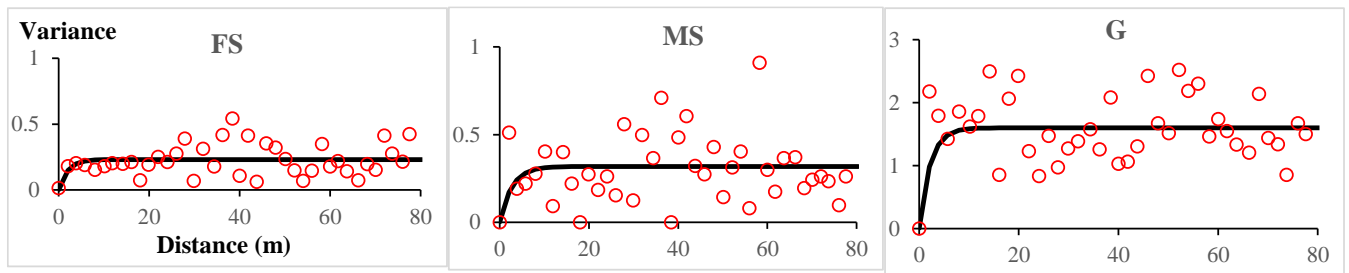
626

627

628

629

**Figure 6**

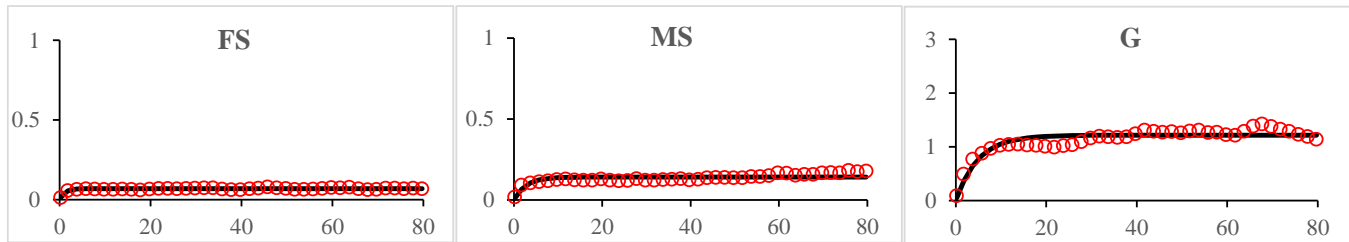


630

631

632

Zone 1

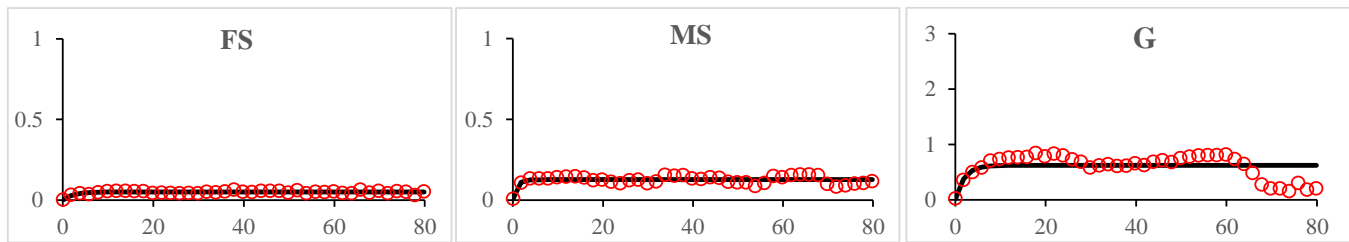


633

634

635

Zone 2



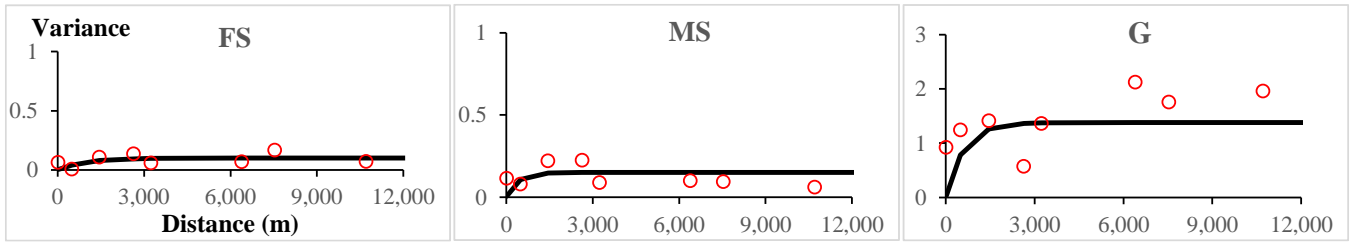
636

637

638

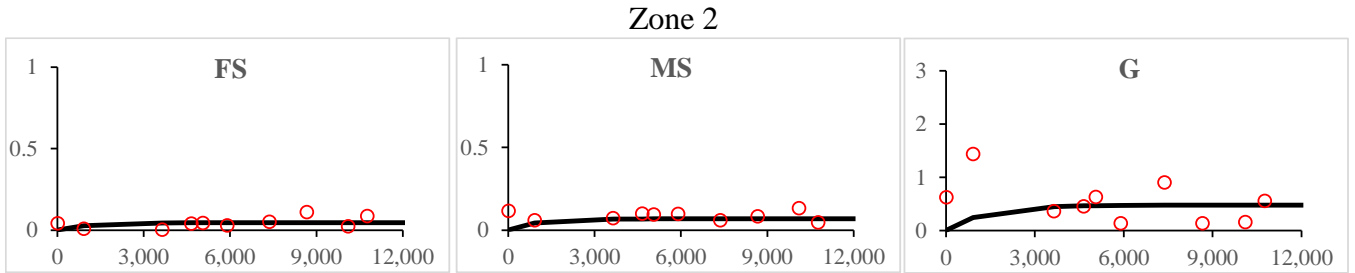
Zone 3

639 **Figure 7**



640

641



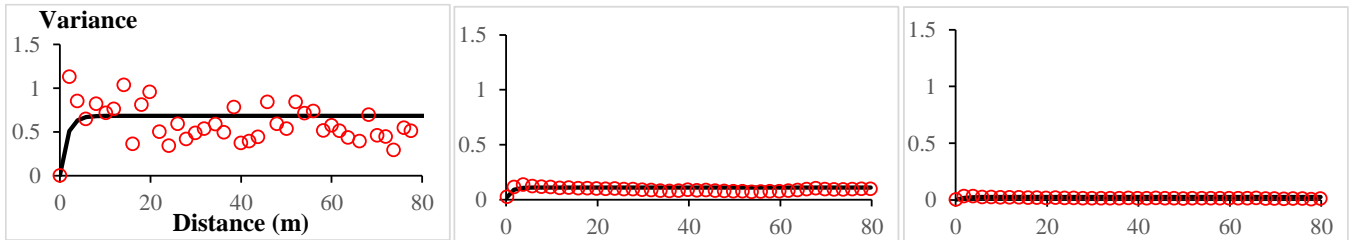
642

643

644

Zone 3

645 **Figure 8**



646

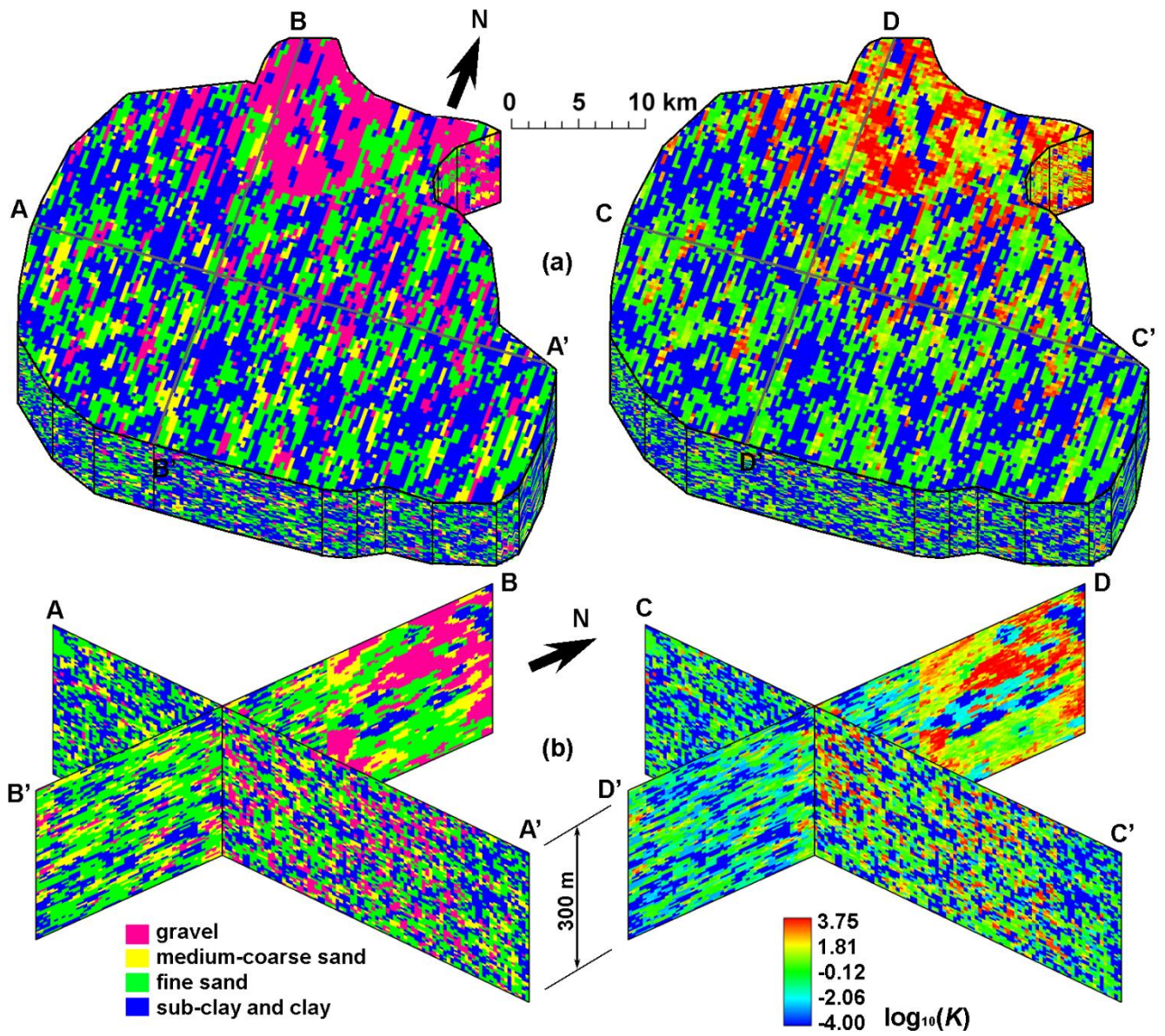
647

648

649

650

651



653

654

655